

## On the Chemical Stability of Post-Lithiated Garnet Al-Stabilized $\text{Li}_7\text{La}_3\text{Zr}_2\text{O}_{12}$ Solid State Electrolyte Thin Films

*Michael Rawlence<sup>1,2</sup>, Inigo Garbayo<sup>2</sup>, Stephan Buecheler<sup>1</sup>, J.L.M. Rupp<sup>2</sup>*

[ 1 ] Lab Thin Films & Photovoltaics, Empa Swiss Fed Labs Material Science & Technology, CH-8600 Dübendorf, Switzerland

[ 2 ] Electrochemical Materials, ETH Zurich, CH-8093 Zurich, Switzerland

### Abstract

Garnet-based Al-doped  $\text{Li}_7\text{La}_3\text{Zr}_2\text{O}_{12}$  has the potential to be used as a solid state electrolyte for future lithium microbattery architectures, due to its relatively high  $\text{Li}^+$  conductivity and stability against Li. Through this work, a model experiment is presented in which the effect of post-lithiation on phase formation and thermodynamic stability is studied for pulsed laser deposited Al-doped  $\text{Li}_7\text{La}_3\text{Zr}_2\text{O}_{12}$  thin films on MgO substrates. We report the implications of the newly suggested post-lithiation route for films with thicknesses between 90 and 380 nm. The phase changes from cubic, to a mix of cubic and tetragonal  $\text{Li}_7\text{La}_3\text{Zr}_2\text{O}_{12}$ , to a cubic  $\text{Li}_7\text{La}_3\text{Zr}_2\text{O}_{12}$  and  $\text{La}_2\text{Zr}_2\text{O}_7$  containing film is accompanied by a reduction in the degree of de-wetting as the thickness increases. This study reveals that the thicker, dense, and continuous films remain predominantly in a mixed phase containing cubic  $\text{Li}_7\text{La}_3\text{Zr}_2\text{O}_{12}$  and the lithium free  $\text{La}_2\text{Zr}_2\text{O}_7$  phase whereas the thinner, de-wetted films exhibit improved lithium incorporation resulting in the absence of the lithium free phase. For tuning the electrical conductivity and effective use of these structures in future batteries, understanding this material system is of great importance as the thermodynamic stability of the cubic  $\text{Li}_7\text{La}_3\text{Zr}_2\text{O}_{12}$  phase in the thin film system will

control its effective use. We report a conductivity of  $1.2 \times 10^{-3} \text{ Scm}^{-1}$  at  $325^\circ\text{C}$  for a 380 nm thick solid state electrolyte film on MgO for potential operation in future all solid state battery assemblies.

## 1. Introduction

All solid state lithium ion batteries offer several advantages over their liquid electrolyte battery counterparts because of their high energy density, cycling stability, and safety. Although prototypes of solid-state batteries do exist, the key improvement required for these batteries to reach their full potential is the development of dense layers of electrolyte materials which block electrons and have fast lithium ion transport. The lithium ion conducting garnet structure  $\text{Li}_7\text{La}_3\text{Zr}_2\text{O}_{12}$  (LLZO) holds promise for application as a solid state electrolyte for all solid state batteries.<sup>1</sup> Advantages include a lithium ion conductivity of up to  $1.32 \times 10^{-3} \text{ Scm}^{-1}$ <sup>2</sup> measured at room temperature on a macrocrystalline pellet, among the highest for solid state electrolytes, and a high stability vs. lithium metal<sup>3,4</sup> and high voltage-cathode materials.<sup>5,6</sup> LLZO exists in two principal crystalline phases, tetragonal (space group  $\text{I4}_1/\text{acd}$ )<sup>7,8</sup> and cubic (space groups  $\text{Ia-3d}$  and  $\text{I-43d}$ ),<sup>9,10</sup> of which cubic  $\text{Ia-3d}$  is the more conductive phase by two orders of magnitude. Furthermore, substitution on the lithium and zirconium sites offer a promising strategy to stabilize the high conductive cubic phase at room temperature and raise the lithium ion conductivity further still.<sup>11-13</sup> The most common doping method is aliovalent substitution of  $\text{Li}^+$  with  $\text{Al}^{3+}$  which improves the ionic conductivity in LLZO by stabilizing the cubic phase, creating additional lithium vacancies in the lattice.<sup>4,14-25</sup>

Although excellent lithium ion conductivities have been achieved for bulk pellets of LLZO based on classic sintering, transferring the material to thin film structures as novel microbattery electrolytes still remains a challenge today. Reviewing literature it can be seen that most popular among the other state-of-the-art solid state electrolytes are LIPON,<sup>26</sup>  $\text{Li}_{3x}\text{La}_{(2/3)-x}\text{TiO}_3$ <sup>27,28</sup> and  $\text{Li}_{10}\text{GeP}_2\text{S}_{12}$ <sup>29</sup> However, here it reported that these solid state electrolytes are not chemically stable against lithium metal which is a highly important property for developing solid state batteries with a high energy density. Therefore,

LLZO electrolytes offer a unique set of properties which can enable the development of high performance all solid state microbatteries.

Work thus far on LLZO processed as thin films has struggled to demonstrate the stabilization of phase pure cubic LLZO with only one clear success using MOCVD.<sup>30</sup> Other techniques used include pulsed laser deposition (PLD)<sup>31,32</sup>, magnetron sputtering,<sup>33</sup> aerosol assisted deposition<sup>34</sup> and sol-gel deposition combined with post annealing.<sup>35,36</sup> Lithium ion conductivities range from  $1 \times 10^{-8} \text{ Scm}^{-1}$ <sup>34</sup> to  $1.6 \times 10^{-6} \text{ Scm}^{-1}$  at room temperature with the recent record conductivity achievement for LLZO thin films deposited by PLD at 600°C were achieved by the groups of Doeff and Hong,<sup>37</sup> although the film appeared to be in phase mixture of tetragonal, cubic LLZO and the de-lithiated impurity phase  $\text{La}_2\text{Zr}_2\text{O}_7$ .

An explanation for the critical difference of two orders of magnitude between sintered pellet and thin film conductivities is still missing in the field and is required in order to develop a clear road map towards microbattery integration. Scrutinizing the literature reports, we conclude the following causes for the varied lithium ion conductivities for thin film LLZO electrolytes:

The first and most crucial point is the stabilization of the correct phase. For processing of the vacuum-based films ablation of sintered pellets is predominantly used. Although the pellet may have the desired chemistry and phase, transfer of the structures to thin films can result in lithium loss and subsequent phase-destabilization during thin film growth due to the volatility of lithium and the high laser energy required. This explains the challenges in growing cubic LLZO thin films by PLD according to references.<sup>31,32,37</sup> On the other hand, turning to wet-chemical film depositions avoids using high laser energies and even sintering, but it is well known that classic wet-chemical oxide film depositions have several additional factors to consider such as the chain length and number of cations in the organic precursors which can influence the degree of crystallization and stabilization of the phases.<sup>38</sup> Despite this general knowledge detailed parameter studies are still missing in the field of LLZO wet-chemical film processing.

Secondly, the morphology of the reported films vary from dense and crack free to highly porous, as in the case of sol-gel deposited films where outgassing organics can cause pores and cracks to form. Reviewing the current literature it can be concluded that there is a strong dependence of the morphology

on the processing method used with vacuum deposition methods generally resulting in higher film densities and phase purities.<sup>31,32</sup> The formation of cationic segregates may also influence the surface morphology and porosity as evident for many other oxide-based thin films.<sup>39,40</sup> To the best of our knowledge studies on surface segregations and its effect on surface film morphologies and chemistry have not been published for LLZO thin films.

Thirdly, the effect of lithium concentration on ionic conductivity is complex and depends on several parameters such as the effective doping level and structural lithium site occupancy ratios between tetragonally and octahedrally coordinated sites.<sup>20</sup> Other factors may also play a role in changing lithium concentrations such as the segregation of lithium and aluminium to the surface, thereby changing the active lithium concentration as observed in pellets of LLZO.<sup>41</sup> It is well known in literature that cationic surface segregation can also strongly affect the ionic conductivity of oxides.<sup>42,43</sup> As lithium is highly volatile in nature and its loss is compensated by chemistry and phase changes, further studies are crucial to shed light on how to best process LLZO thin films for future garnet-electrolyte based microbatteries and to optimize electrolyte-electrode lithium transfer for large-scale battery systems. Thus far the extent of Li loss resulting from vacuum and high temperature processing of LLZO based thin films is unknown. The lack of this type of data in the field is most likely due to the difficulty of measuring Li particularly in thin films. Methods such as elastic recoil detection analysis (ERDA), inductively coupled plasma atomic emission spectroscopy (ICP-OES), and nuclear reaction analysis (NRA) could be utilised in this direction.

Lattice strain may play a significant role, in other thin film systems strain can alter ionic conductivity by orders of magnitude.<sup>44,45</sup> We summarize that the influence of lattice strain imposed by the substrate is still unknown for LLZO thin films and could alter the phase stability as well as cationic segregation. Finally we consider the importance of size-dependent phase transformations in which the reduction of particle size to the sub 100 nm scale increases the influence of the surface energy and induces a phase change. For the LLZO system one recent study exhibited this effect showing that the surface energy of cubic-LLZO is greater than tetragonal-LLZO and therefore a reduction in particle size led to the

stabilization of cubic-LLZO.<sup>46</sup> This phenomenon is also demonstrated in other phase polymorphous ceramics such as titania<sup>47</sup> and zirconia.<sup>48-51</sup>

In this work, we provide guidance for phase stabilization and microstructural development of Al:LLZO thin films and suggest a novel post-lithiation step to be incorporated subsequent to classic vacuum deposition (PLD). The crystallization and phase development are carefully analysed in the formation of continuous, dense, and crack-free Al:LLZO thin films and observations are coupled with microstructural thin film changes. Finally, we conclude on the thermodynamic stability and the impact of the post-lithiation treatment for the Al:LLZO thin films prepared by PLD regarding their lithium ion conductivity using electrochemical impedance spectroscopy, which is an important step towards integrating them as solid state electrolytes in future microbatteries.

## 2. Experimental

### **Thin Film Preparation by Pulsed Laser Deposition and Post-Lithiation-Annealing for Al doped Lithium Lanthanum Zirconate Electrolytes**

To create a target for ablation in pulsed laser deposition, a pellet with the target composition  $\text{Li}_{6.22}\text{La}_3\text{Zr}_2\text{Al}_{0.26}\text{O}_{12}$ , henceforth referred to as Al:LLZO, was synthesised using a sol-gel Pechini synthesis route. Precursor salts were measured in stoichiometric quantities with an additional molar 10% of lithium: For this,  $\text{Li}_2\text{CO}_3$  (Alfa Aesar, 99%),  $\text{La}(\text{NO}_3)_3 \cdot 6\text{H}_2\text{O}$ , (Alfa Aesar, >99.9%),  $\text{Zr}(\text{C}_5\text{H}_7\text{O}_2)_4$  (Alfa Aesar), and  $\text{Al}(\text{NO}_3)_3 \cdot 9\text{H}_2\text{O}$  (Fluka, >99%) were dissolved into water with added  $\text{HNO}_3$  to keep the cations in solution. Citric acid and ethylene glycol were added to the solution to act as the complexing and polymerising agent, respectively. The solution was left to polymerise for 6 hours at  $110^\circ\text{C}$  then fired at  $900^\circ\text{C}$  for 10 hours in dry  $\text{O}_2$  to burn off the organic components and form tetragonal Al:LLZO. The resulting powder was ground by hand then isostatically pressed with an additional 10 mol% of  $\text{Li}_2\text{O}$  (Alfa Aesar, 99.9%) at 1000 MPa. Finally the pellet was covered in parent powder and sintered at  $1050^\circ\text{C}$  for 10 hours in dry  $\text{O}_2$  to form the cubic phase. Pellets were 25 mm in diameter and had a theoretical density of 90% ( $5.022 \text{ gcm}^{-3}$  is the maximum). Alumina crucibles and

plates were used for high temperature processes, which may slightly alter the final Al content in the pellet. However, this effect was considered to be negligible as the cubic garnet phase was successfully stabilized with no impurities, Fig. S1. Grinding and handling of powders was done within a custom designed glovebox set up for solid state battery cells (Inert, USA, and Electrochemical Materials, ETH) under Ar gas with <2ppm water and O<sub>2</sub> levels to limit exposure to moisture.

Thin films were deposited by pulsed laser deposition (PLD, Surface Technologies, Germany; KrF laser, 248 nm) with a laser energy of 0.54 J cm<sup>-2</sup> per pulse and a pulse frequency of 10 Hz. Additionally an O<sub>2</sub> partial pressure of 10 mTorr and substrate temperature of 50°C were maintained. Films were deposited onto square, single crystal, (100)-oriented, double-side polished, MgO (Crystec, Germany) kept at a target-substrate distance of 65 mm. Film thicknesses were estimated based on a calibration connecting the number of shots based on fixed laser conditions with resultant film thickness observed via SEM cross-section analyses.

The method used for post-annealing the films under a lithium partial pressure to avoid lithium losses or segregation at temperature is shown schematically in Fig. 1. An alumina crucible with a 20 mm diameter contains the film and 100 mg of Li<sub>2</sub>O powder which readily converts to LiOH in air. The crucible was then sealed in air with ceramic glue (Thermokitt Roth, Carl Roth GmbH, Germany) and annealed at 600°C for 24h under a flow of oxygen. During this time, the LiOH melts and creates lithium rich atmosphere.

### **Structural and Electrochemical Investigation of Al doped Lithium Lanthanum Zirconate Thin Films**

In order to identify the crystallographic phase, X-ray diffraction (XRD) was carried out using a Bruker D8-diffractometer using a Cu source with K<sub>α1</sub> wavelength at an accelerating voltage of 40 keV with Bragg-Brentano geometry for pellets and grazing incidence geometry for thin films. Scanning Electron Microscopy using an FEI Nova NanoSEM 230 at 2 to 5 keV was conducted on thin films using a 5 nm sputtered platinum coating to mitigate charging effects.

For electrochemical studies 100 nm thick gold contacts were deposited onto the film using thermal evaporation (Plassys II, France) through a custom made, laser cut, stainless steel shadow mask with a minimum electrode separation of 250  $\mu\text{m}$ . A 2-point electrode geometry was used for electrochemical impedance spectroscopy (EIS) (Zahner, Germany) to probe the AC ionic conductivity over a range of temperatures, during both heating and cooling, with an alternating voltage of  $\pm 50$  mV and frequency range between  $1 \times 10^6 - 0.1\text{Hz}$ . The sample was measured on a Linkam stage (HFS-600E, UK) with Au-coated tungsten microprobes and electric measurements were carried out in a constant synthetic air gas flow of 40 sccm. Temperature was directly measured on the sample surface with a K-type thermocouple.

### **3. Results and Discussion**

#### **3.1 Al Doped Lithium Lanthanum Zirconia Thin Film Electrolytes without Post-Lithiation: As-Deposited PLD Film**

The microstructure and morphology of  $\text{Li}_7\text{La}_3\text{Zr}_2\text{O}_{12}$  based thin films processed by pulsed laser deposition at  $50^\circ\text{C}$  were investigated directly after deposition, Fig. 2. Here, the examination of the as-deposited  $\text{Li}_7\text{La}_3\text{Zr}_2\text{O}_{12}$  thin film microstructure by SEM reveals the successful deposition of a dense and crack-free thin film with an indication of particulate ejection during processing, common in PLD depositions,<sup>52</sup> Fig. 2a. The cross section of the same film confirms the dense microstructure, Fig. 2b. We conclude based on the SEM cross-section an average film thickness in the range of  $320 \pm 15$  nm with a tendency for columnar grain growth in its microstructure. We investigate the crystallinity of the as-deposited PLD film via XRD, Fig. 2c. Here, we measure a single broadened diffraction peak ranging from  $21^\circ$  to  $35^\circ$  for the film as deposited at  $50^\circ\text{C}$ . There are also some low intensity peaks besides the broadened peak which can be assigned to the (211), (321), (420), (422), (532), and (642) miller indices of the bulk polycrystalline cubic- $\text{Li}_7\text{La}_3\text{Zr}_2\text{O}_{12}$  (c-LLZO) phase, in accordance with literature.<sup>23</sup> The results are in agreement with earlier PLD studies on LLZO film formation by Park et al.<sup>37</sup> who also used an  $\text{O}_2$  pressure of 10 mTorr during deposition but three times the laser fluence at  $1.5 \text{ J cm}^{-2}$ .

### 3.2 Post-Lithiated and Annealed PLD Films of Al-Doped Lithium Lanthanum Zirconate Films: Structural and Morphological Analysis

As PLD deposition is a technique which can cause a lower relative yield of lithium due to material being re-sputtered from the film surface and the high volatility of lithium in a vacuum,<sup>53</sup> and a high proportion of lithium is essential for crystallization of the garnet LLZO (see Afyon<sup>54</sup> and Rettenwander<sup>55</sup> for detailed discussions) we subject the films to a lithium post-annealing step after PLD deposition. The films are annealed on the one hand to ensure sufficient crystallization to switch from amorphous to long range order, and on the other hand to ensure enough lithium is present for LLZO to form by providing excess lithium powder in the closed crucible at high temperatures. Thus far for PLD processing of LLZO films this route was not considered and standard annealing often lead to the formation of lithium free phases at higher temperatures.<sup>31,37</sup>

We study a series of films with increasing thickness from 90 to 380 nm, which were subjected to the lithium post-annealing treatment after PLD, and analyse the microstructures with SEM shown in Fig. 3 and X-ray diffraction in Fig. 4. All films were annealed under the same conditions of 600°C for 24h in the presence of a LiOH reservoir.

In Fig. 3 the scanning electron micrographs show a clear progression in the microstructure from the formation of separate islands for the film of 90 nm thickness, Fig. 3a, to more continuous patches of de-wetted material for the 110 nm thick film, Fig. 3b. Moving to 130 nm thickness results in a fully continuous film microstructure of more dense material with nano-sized crystallites on the surface, Fig. 3c. At 380 nm the film is continuous and has similar density to the 130 nm film, however, a roughened surface is observable with features several microns across on the film surface.

We now assess the crystallinity and formation of phases of the films of varying thicknesses via X-ray diffraction, Fig. 4. The 90 nm thick film is of cubic LLZO phase, indicated by the presence of all diffraction indices of (211), (220), (321), (440), (420), (422), (211), (521), (640), (721), and (642), Fig. 4a. This single c-LLZO phase is in good agreement with literature for polycrystalline pellets.<sup>23</sup> In addition, a small amount of  $\text{Li}_2\text{CO}_3$  formed during the processing is measurable, in agreement with



earlier reports on bulk pellet surface reactions.<sup>56</sup> We attribute this to the reaction of excess LiOH on the surface of the film reacting with CO<sub>2</sub> in the air during post-process characterisation and can observe this in some of the following microstructures as well. A slight increase in film thickness to the 110 nm thick structure, results in the formation of a mixed phase including both tetragonal and cubic LLZO, Fig. 4b. For the 130 nm thick film, one observes the cubic LLZO phase in combination with the lithium deficient La<sub>2</sub>Zr<sub>2</sub>O<sub>7</sub> (LZO) pyrochlore phase.<sup>57</sup> The increase in LZO phase coupled with the reduction in LLZO suggests that the pyrochlore phase forms at the expense of the tetragonal/cubic LLZO phases, Fig. 4c. At 380 nm film thickness the majority of the film has formed into LZO while a small quantity of cubic LLZO is noted, Fig. 4d. Additional surface impurity phases of Li<sub>2</sub>CO<sub>3</sub> are also measurable. By analysing the FWHM, it is apparent that the crystal size in the all the films is on the nanoscale. Furthermore the LLZO majority films appear to have a smaller grain size than the thicker LZO containing films.

We interpret the morphological and phase changes in the Al-Li-La-Zr-O thin film microstructure as follows in light of the post-lithiation annealing treatment and effective lithiated film volumes:

Firstly, at small film thickness up to 90 nm a pure bulk c-LLZO film prevails. In this state the film reveals a degree of lithiation per film volume in the correct range for stabilizing the cubic-LLZO phase, Fig. 3a and Fig. 4a. Too little lithium would result in the formation of the LZO whereas a lithium excess would cause the formation of other lithium rich phases such as AlLiO<sub>2</sub> and LaAlO<sub>3</sub>.<sup>22</sup> Here, the films appear to have a high surface tension due to the surface energy difference between the MgO substrate and film. Island formation is the result of the minimization of the surface energy during annealing, and in addition, Ostwald ripening may contribute to the formation of the islands shown in the scanning electron micrographs, Fig. 3a.

Secondly, we observe an intermediate state at which both the tetragonal and cubic phases co-exist for the film thickness of 110 nm, Fig. 3b and Fig 4b. One hypothesis could be that the film compensates a part of the internal stress by a phase transformation from cubic to tetragonal and therefore a lesser degree of the previous sub-micron island structures are observed resulting in the formation of more connected film patches. Although these results are of great interest due to the formation of LLZO with

no trace of the delithiated LZO, to the best of our knowledge we cannot compare our new findings to other film literature on LLZO film formation based on missing model experiments in the field studying the degree of lithiation in thin films.

Thirdly, for larger film thicknesses above 110 nm the post-lithiation step is not sufficient to lithiate the whole bulk volume consistently, Fig. 3c, d and Fig. 4c and d. The trend shows that as the thickness increases, the transition from a largely amorphous film to co-existing tetragonal and cubic LLZO phases, instead forms the lithium deficient  $\text{La}_2\text{Zr}_2\text{O}_7$  (LZO) phase, Fig. 4c, d. In this phase transition the film maintains a much higher density and a continuous film microstructure is displayed, Fig. 3c, d. This finding of lower lithium contents for film above the threshold of 110nm has also been noted in a paper by Park et. al. where small quantities of LLZO were observed on the surface of a thicker film synthesised at a temperature of 700°C which was otherwise mainly composed of LZO.<sup>37</sup>

In summary, we report that there is currently a compromise between forming a higher density film microstructure and achieving thermodynamic stability of the c-LLZO phase, which depends crucially on the degree of lithiation per volume in the chemistry of the film structure. We demonstrate a range of thermodynamic transition from single bulk phase c-LLZO with disconnected and de-wetted islands forming on an MgO substrate, to an intermediate mixed t/c-LLZO phase, leading to a c-LLZO and lithium deficient LZO phase mixture with a continuous and crack-free morphology and a lower lithium content to volume ratio. We observe a fine balance between the formation of each phase and their surface energies, exhibited by de-wetting of the film microstructures. Importantly the results suggest that during the post-lithiation synthesis step lithium incorporation into the film is inhibited since the largest film thicknesses are the ones revealing the lowest incorporation of structural lithium. Both the increase in surface area and the smaller grain size in the 90 nm and 110 nm films could have affected the ability of the films to absorb lithium. A larger surface area would result in a higher surface reaction rate and the presence of more grain boundary interfaces exposed to the surface could improve the lithium in-diffusion. Judging from these experiments it is evident that stabilizing pure c-LLZO in dense thin film microstructures is challenging on the MgO substrate. Hence, we have chosen the mixture of c-LZZO/LZO for electrochemical characterization as it is dense and could therefore be realistically

integrated into a microbattery. We compare this model experiment showing the range of phase changes to a report on phase occurrences in Al:LLZO PLD films mostly discussing polycrystalline films on phase mixtures of c-LLZO/LZO see Park et al.<sup>37</sup>

### **3.3 Electrical Conductivity of Al Doped Lithium Lanthanum Zirconia Thin Films: Effect of Lithiation and Phase**

To measure the effectiveness of the lithiation treatment post-PLD, we measure the electrochemical properties of the 380 nm film and compare to literature. We utilize the classic 2-probe geometry with gold electrodes for in-plane electrochemical impedance spectroscopy measurements. An example of the electrochemical impedance response obtained for the 380 nm thick c-LLZO/LZO film is given in Fig. 5a, in a Nyquist plot representation measured at 240°C and 450°C in dry synthetic air. In general, a clear impedance arc is measured at higher frequencies, which is attributed to the bulk resistance of the film. A second semicircle is also generally observed towards the lower frequencies, most probably associated to the grain boundary contribution. Finally, at high temperatures the blocking Au electrode contribution is clearly differentiated. The impedance data was fitted using an equivalent circuit with a single RC component for the high frequency part, denoting the bulk resistance of the film. At 325°C this resulted in a lithium ion bulk conductivity of  $1.2 \times 10^{-3} \pm 0.05 \times 10^{-3} \text{ Scm}^{-1}$  as compared to  $\sim 1.7 \times 10^{-3} \text{ Scm}^{-1}$  for Park et. al. in the same temperature range.<sup>37</sup>

In an Arrhenius type plot we compare the films of c-LLZO/LZO synthesized via PLD and post-lithiation in this work to literature, Fig. 5b. The 380 nm thick film reveals two activation energies for ionic conductivity of  $1.39 \pm 0.05 \text{ eV}$  for the temperatures range of 25 to 300°C and a lowered one of  $0.6 \pm 0.05 \text{ eV}$  for temperatures up to 400°C. Upon cooling, the activation energy returns to the lower value demonstrating a reversible process. The sudden change in activation energy indicates that a different mechanism for ionic transport is dominant in the higher temperature regime. In Fig. 5c a proposed circuit model is presented for interpreting the impedance data. One hypothesis for this behaviour is that at lower temperatures the high activation energy originates from the lithium deficient LZO phase

<sup>58-60</sup> and lithium ion pathways through the bulk of the film become more favourable at temperatures above 300°C. Alternatively a metastable phase with a higher lithium ion conductivity may form at higher temperatures.

The activation energies seen here compare closely to 0.67 eV for polycrystalline c-LLZO/LZO films synthesized by PLD without post-lithiation treatment by Park et. al,<sup>37</sup> and are slightly higher than the PLD-grown epitaxial LLZO reported by Kim et. al. (0.52 eV).<sup>31</sup> We attribute the small differences in bulk conductivity at high temperatures measured between the here synthesized 380 nm thick film and Park's work to slight difference in the quantity of c-LLZO over the non-lithiated LZO phase. Moreover, the greater performance reported by Kim et al. might come from the different film morphology, i.e. polycrystalline films vs. epitaxially grown films.

It is to be noted that based on this impedance study we demonstrate that reasonable conductivities of  $1.2 \times 10^{-3} \text{ Scm}^{-1}$  can be achieved at 325°C, which may be used for operation of microbattery architectures in a mid-to-elevated temperature regime.

#### 4. Conclusion

We have presented this model experiment first in the field of garnet based  $\text{Li}_7\text{La}_3\text{Zr}_2\text{O}_{12}$  thin films to study the interplay of phase formation, microstructural evolution, and thermodynamic stability for  $\text{Li}_7\text{La}_3\text{Zr}_2\text{O}_{12}$  thin films on MgO substrates processed by pulsed laser deposition and a post-lithiation step. For these we investigated the changes in film microstructures relative to film thickness (whereby the effective lithiation per volume is manipulated).

Dense and crack-free amorphous thin film microstructures are synthesized directly after pulsed laser deposition at 50°C. Through annealing at the relatively low temperature of 600°C in the presence of a LiOH partial pressure the films were lithiated to varying degrees. We observe that at low film thicknesses of 90 nm (high lithiation degree per volume) an inhomogeneous film of de-wetted islands on MgO forms, but is composed of the desired highly lithium ion conducting c-LLZO phase. Increasing thickness to 110 nm results in an intermediate combination of cubic and tetragonal LLZO phases still

with a large degree of de-wetting. Finally, we conclude that for film thicknesses of 130 nm and above a phase mixture of c-LLZO and LZO prevails coupled with a sufficiently dense film microstructure for electrochemical operation. Interestingly, there exists a fine balance between the thermodynamic phase stability, degree of lithiation, and degree of de-wetting for the Al-Li-La-Zr-O material in the form of thin films. The large increase in surface area of the thinner films caused by the de-wetting is a strong indication that lithium incorporation is dependent on a surface reaction followed by a lithium diffusion processes on the nanoscale. The challenge is clearly to keep the lithium integrated into the structure, but also to avoid potential inhomogeneities in the film microstructures. Through this work the clear additional challenges of processing and establishment of stable phases and microstructures are revealed when comparing to classic bulk ceramic pellet processing.

Based on our results from the model experiment presented we conclude that for films of thicknesses larger than 130 nm processed by the post-lithiation treatment after pulsed laser deposition, stable and dense structures can be formed suited for conductivity studies in a 2-point geometry with microelectrodes. Electrochemical studies showed a high activation energy of 1.39 eV for the 380 nm film at temperatures below 300°C. Above 300°C a different mechanism for lithium transport emerged with an activation energy of 0.6 eV which was comparable to other LLZO thin films in literature with a phase mixture of c-LLZO/LZO. Here, future work on lithium ion conduction mechanisms in thin films may elucidate further on what we observe in our experiments.

We demonstrate here a systematic transition of the phase formation relative to film thickness which reveals key information on the stability of c-LLZO in thin films. These first reported trends lead the way for further improvement in the processing of LLZO for electrolytes in microbatteries.

## **5. Acknowledgements**

The authors thank the Competence Centre for Energy and Mobility (CCEM) and Swiss Electric Research for funding of the project: Proposal 911 “SLIB - All solid State Li-Ion Batteries based on New Ceramic Li-Ion Electrolytes”.

## 6. References

- (1) Thangadurai, V.; Narayanan, S.; Pinzaru, D. *Chemical Society Reviews* **2014**, *43*, 4714.
- (2) Rettenwander, D.; Redhammer, G.; Preishuber-Pflügl, F.; Cheng, L.; Miara, L.; Wagner, R.; Welzl, A.; Suard, E.; Doeff, M. M.; Wilkening, M.; Fleig, J.; Amthauer, G. *Chemistry of Materials* **2016**, *28*, 2384.
- (3) Wolfenstine, J.; Allen, J. L.; Read, J.; Sakamoto, J. *Journal of Materials Science* **2013**, *48*, 5846.
- (4) Kotobuki, M.; Kanamura, K.; Sato, Y.; Yoshida, T. *Journal of Power Sources* **2011**, *196*, 7750.
- (5) Deng, Y.-F.; Zhao, S.-X.; Xu, Y.-H.; Nan, C.-W. *Journal of Materials Chemistry A* **2014**, *2*, 18889.
- (6) Richards, W. D.; Miara, L. J.; Wang, Y.; Kim, J. C.; Ceder, G. *Chemistry of Materials* **2016**, *28*, 266.
- (7) Wolfenstine, J.; Rangasamy, E.; Allen, J. L.; Sakamoto, J. *Journal of Power Sources* **2012**, *208*, 193.
- (8) Awaka, J.; Kijima, N.; Hayakawa, H.; Akimoto, J. *Journal of Solid State Chemistry* **2009**, *182*, 2046.
- (9) Murugan, R.; Thangadurai, V.; Weppner, W. *Angewandte Chemie-International Edition* **2007**, *46*, 7778.
- (10) Wagner, R.; Redhammer, G. J.; Rettenwander, D.; Senyshyn, A.; Schmidt, W.; Wilkening, M.; Amthauer, G. *Chemistry of Materials* **2016**, *28*, 1861.
- (11) Deviannapoorani, C.; Dhivya, L.; Ramakumar, S.; Murugan, R. *Journal of Power Sources* **2013**, *240*, 18.
- (12) Bernuy-Lopez, C.; Manalastas, W.; del Amo, J. M. L.; Agüadero, A.; Agüesse, F.; Kilner, J. A. *Chemistry of Materials* **2014**, *26*, 3610.
- (13) Rangasamy, E.; Wolfenstine, J.; Allen, J.; Sakamoto, J. *Journal of Power Sources* **2013**, *230*, 261.
- (14) Jin, Y.; McGinn, P. J. *Journal of Power Sources* **2011**, *196*, 8683.
- (15) Geiger, C. A.; Alekseev, E.; Lazic, B.; Fisch, M.; Armbruster, T.; Langner, R.; Fechtelkord, M.; Kim, N.; Pettke, T.; Weppner, W. *Inorganic Chemistry* **2011**, *50*, 1089.
- (16) Awaka, J.; Takashima, A.; Kataoka, K.; Kijima, N.; Idemoto, Y.; Akimoto, J. *Chemistry Letters* **2011**, *40*, 60.
- (17) Li, Y.; Han, J.-T.; Wang, C.-A.; Vogel, S. C.; Xie, H.; Xu, M.; Goodenough, J. B. *Journal of Power Sources* **2012**, *209*, 278.
- (18) Takano, R.; Tadanaga, K.; Hayashi, A.; Tatsumisago, M. *Solid State Ionics* **2014**, *255*, 104.
- (19) Düvel, A.; Kuhn, A.; Robben, L.; Wilkening, M.; Heitjans, P. *The Journal of Physical Chemistry C* **2012**, *116*, 15192.
- (20) David, I. N.; Thompson, T.; Wolfenstine, J.; Allen, J. L.; Sakamoto, J. *Journal of the American Ceramic Society* **2015**, *98*, 1209.
- (21) Rosenkowitz, N.; Schuhmacher, J.; Bockmeyer, M.; Deubener, J. *Journal of Power Sources* **2015**, *278*, 104.
- (22) Rangasamy, E.; Wolfenstine, J.; Sakamoto, J. *Solid State Ionics* **2012**, *206*, 28.
- (23) Buschmann, H.; Dolle, J.; Berendts, S.; Kuhn, A.; Bottke, P.; Wilkening, M.; Heitjans, P.; Senyshyn, A.; Ehrenberg, H.; Lotnyk, A.; Duppel, V.; Kienle, L.; Janek, J. *Physical Chemistry Chemical Physics* **2011**, *13*, 19378.
- (24) Raskovalov, A. A.; Il'ina, E. A.; Antonov, B. D. *Journal of Power Sources* **2013**, *238*, 48.
- (25) Shimonishi, Y.; Toda, A.; Zhang, T.; Hirano, A.; Imanishi, N.; Yamamoto, O.; Takeda, Y. *Solid State Ionics* **2011**, *183*, 48.

- (26) Yu, X. H.; Bates, J. B.; Jellison, G. E.; Hart, F. X. *Journal of the Electrochemical Society* **1997**, *144*, 524.
- (27) Chen, C. H.; Amine, K. *Solid State Ionics* **2001**, *144*, 51.
- (28) Aguesse, F.; Roddatis, V.; Roqueta, J.; Garcia, P.; Pergolesi, D.; Santiso, J.; Kilner, J. A. *Solid State Ionics* **2015**, 272, 1.
- (29) Mo, Y.; Ong, S. P.; Ceder, G. *Chemistry of Materials* **2012**, *24*, 15.
- (30) Katsui, H.; Goto, T. *Thin Solid Films* **2015**, *584*, 130.
- (31) Kim, S.; Hirayama, M.; Taminato, S.; Kanno, R. *Dalton Transactions* **2013**, 42, 13112.
- (32) Tan, J. J.; Tiwari, A. *Ecs Solid State Letters* **2012**, *1*, Q57.
- (33) Kalita, D. J.; Lee, S. H.; Lee, K. S.; Ko, D. H.; Yoon, Y. S. *Solid State Ionics* **2012**, 229, 14.
- (34) Ahn, C. W.; Choi, J. J.; Ryu, J.; Hahn, B. D.; Kim, J. W.; Yoon, W. H.; Choi, J. H.; Park, D. S. *Journal of the Electrochemical Society* **2015**, *162*, A60.
- (35) Tadanaga, K.; Egawa, H.; Hayashi, A.; Tatsumisago, M.; Mosa, J.; Aparicio, M.; Duran, A. *Journal of Power Sources* **2015**, 273, 844.
- (36) Chen, R.-J.; Huang, M.; Huang, W.-Z.; Shen, Y.; Lin, Y.-H.; Nan, C.-W. *Journal of Materials Chemistry A* **2014**, *2*, 13277.
- (37) Park, J. S.; Cheng, L.; Zorba, V.; Mehta, A.; Cabana, J.; Chen, G. Y.; Doeff, M. M.; Richardson, T. J.; Park, J. H.; Son, J. W.; Hong, W. S. *Thin Solid Films* **2015**, 576, 55.
- (38) Rupp, J. L. M.; Scherrer, B.; Gauckler, L. J. *Physical Chemistry Chemical Physics* **2010**, *12*, 11114.
- (39) Huber, T. M.; Opitz, A. K.; Fleig, J. *Solid State Ionics* **2015**, 273, 8.
- (40) Ryll, T.; Galinski, H.; Schlagenhauf, L.; Elser, P.; Rupp, J. L. M.; Bieberle-Hutter, A.; Gauckler, L. J. *Advanced Functional Materials* **2011**, *21*, 565.
- (41) Cheng, L.; Park, J. S.; Hou, H.; Zorba, V.; Chen, G.; Richardson, T.; Cabana, J.; Russo, R.; Doeff, M. *Journal of Materials Chemistry A* **2014**, *2*, 172.
- (42) Chen, Y.; Téllez, H.; Burriel, M.; Yang, F.; Tsvetkov, N.; Cai, Z.; McComb, D. W.; Kilner, J. A.; Yildiz, B. *Chemistry of Materials* **2015**, *27*, 5436.
- (43) Kubicek, M.; Cai, Z. H.; Ma, W.; Yildiz, B.; Hutter, H.; Fleig, J. *Acs Nano* **2013**, *7*, 3276.
- (44) Schweiger, S.; Kubicek, M.; Messerschmitt, F.; Murer, C.; Rupp, J. L. M. *Acs Nano* **2014**, *8*, 5032.
- (45) Shi, Y. U.; Bork, A. H.; Schweiger, S.; Rupp, J. L. M. *Nature Materials* **2015**, *14*, 721.
- (46) Yang, T.; Gordon, Z. D.; Li, Y.; Chan, C. K. *Journal of Physical Chemistry C* **2015**, *119*, 14947.
- (47) Gribb, A. A.; Banfield, J. F. *American Mineralogist* **1997**, *82*, 717.
- (48) Zhang, Y. L.; Jin, X. J.; Rong, Y. H.; Hsu, T. Y.; Jiang, D. Y.; Shi, J. L. *Materials Science and Engineering a-Structural Materials Properties Microstructure and Processing* **2006**, 438, 399.
- (49) Scherrer, B.; Heiroth, S.; Hafner, R.; Martynczuk, J.; Bieberle-Hutter, A.; Rupp, J. L. M.; Gauckler, L. J. *Advanced Functional Materials* **2011**, *21*, 3967.
- (50) Frison, R.; Heiroth, S.; Rupp, J. L. M.; Conder, K.; Barthazy, E. J.; Muller, E.; Horisberger, M.; Dobeli, M.; Gauckler, L. J. *Solid State Ionics* **2013**, 232, 29.
- (51) Scherrer, B.; Martynczuk, J.; Galinski, H.; Grolig, J. G.; Binder, S.; Bieberle-Hutter, A.; Rupp, J. L. M.; Prestat, M.; Gauckler, L. J. *Advanced Functional Materials* **2012**, *22*, 3509.
- (52) D.B. Crissey, G. K. H. *Wiley-Interscience* **1994**.
- (53) Schou, J. *Applied Surface Science* **2009**, 255, 5191.
- (54) Afyon, S.; Krumeich, F.; Rupp, J. L. M. *Journal of Materials Chemistry A* **2015**, *3*, 18636.
- (55) Rettenwander, D.; Langer, J.; Schmidt, W.; Arrer, C.; Harris, K. J.; Terskikh, V.; Goward, G. R.; Wilkening, M.; Amthauer, G. *Chemistry of Materials* **2015**, *27*, 3135.
- (56) Cheng, L.; Wu, C. H.; Jarry, A.; Chen, W.; Ye, Y.; Zhu, J.; Kostecki, R.; Persson, K.; Guo, J.; Salmeron, M.; Chen, G.; Doeff, M. *ACS Applied Materials & Interfaces* **2015**, *7*, 17649.

- (57) Kong, L.; Karatchevtseva, I.; Gregg, D. J.; Blackford, M. G.; Holmes, R.; Triani, G. *Journal of the American Ceramic Society* **2013**, 96, 935.
- (58) Ou, G.; Liu, W.; Yao, L.; Wu, H.; Pan, W. *Journal of Materials Chemistry A* **2014**, 2, 1855.
- (59) Islam, Q. A.; Nag, S.; Basu, R. N. *Materials Research Bulletin* **2013**, 48, 3103.
- (60) Labrincha, J. A.; Frade, J. R.; Marques, F. M. B. *Solid State Ionics* **1997**, 99, 33.

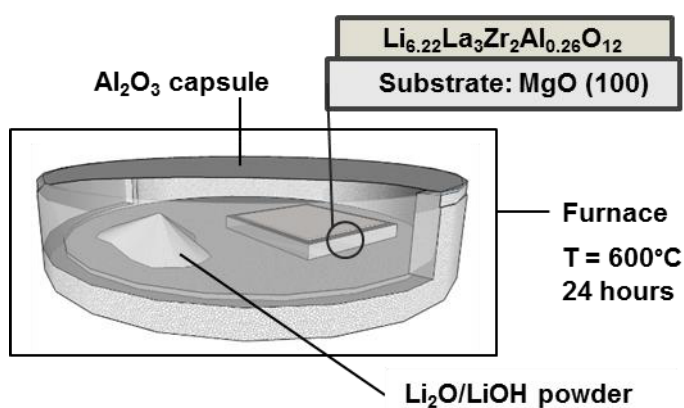


Fig. 1 Schematic of thin film annealing setup. The  $\text{Al}_2\text{O}_3$  capsule is shown partly transparent to reveal the Li source powder and thin film inside.



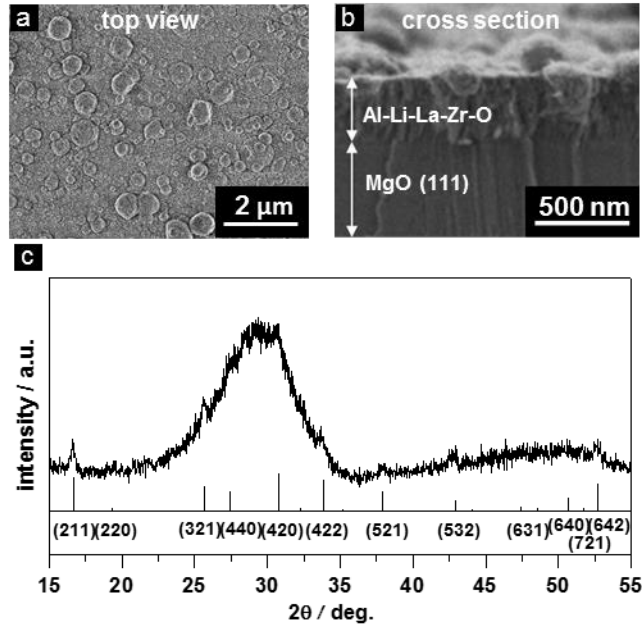


Fig. 2 An as-deposited  $\text{Li}_7\text{La}_3\text{Zr}_2\text{O}_{12}$  based thin film deposited on a single crystal MgO substrate at 50°C by PLD (a) top view SEM micrograph and (b) cross-sectional SEM micrograph. (c) XRD pattern of amorphous thin film structure and comparison to reference  $\text{Li}_7\text{La}_3\text{Zr}_2\text{O}_{12}$  cubic structure.

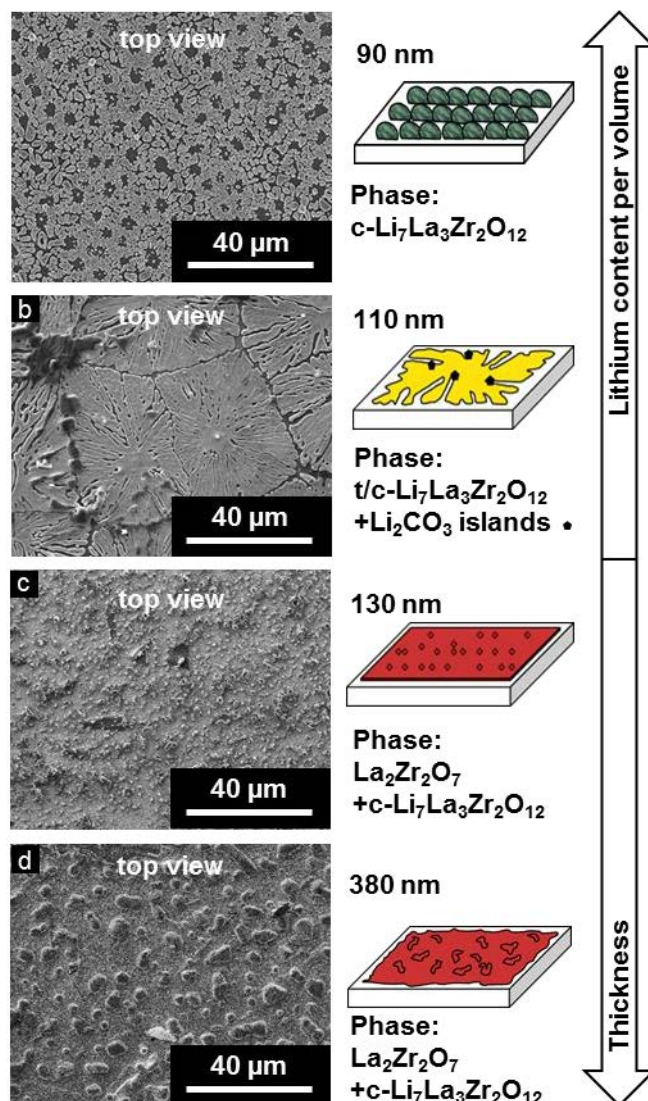


Fig. 3 SEM micrographs of  $\text{Li}_7\text{La}_3\text{Zr}_2\text{O}_{12}$  thin film series of increasing thickness a) 90 nm b) 110 nm c) 130 nm d) 380 nm. Accompanying schematics combine information from Fig. 3 and 4 to show the progression of phase and morphology as the thickness is increased. All films are deposited on MgO and post annealed with the lithium treatment.

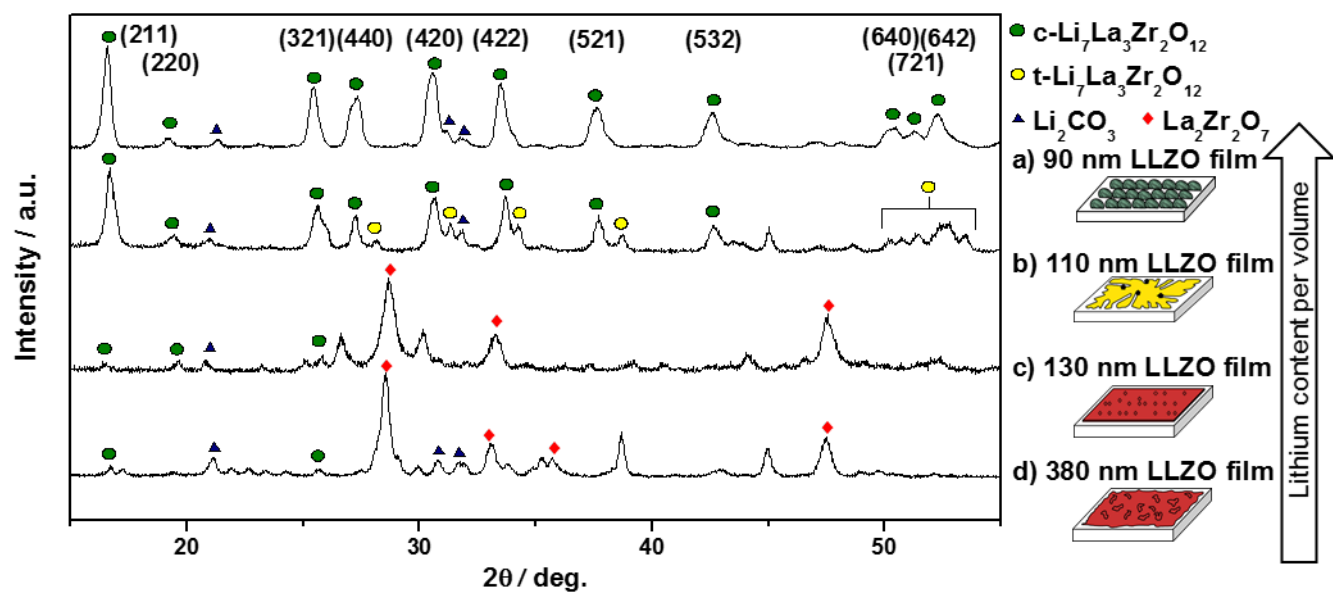


Fig. 4 XRD of  $\text{Li}_7\text{La}_3\text{Zr}_2\text{O}_{12}$  film series of increasing thickness. Miller indices are of the c- $\text{Li}_7\text{La}_3\text{Zr}_2\text{O}_{12}$  phase. Other symbols denote impurity phases present in the films.

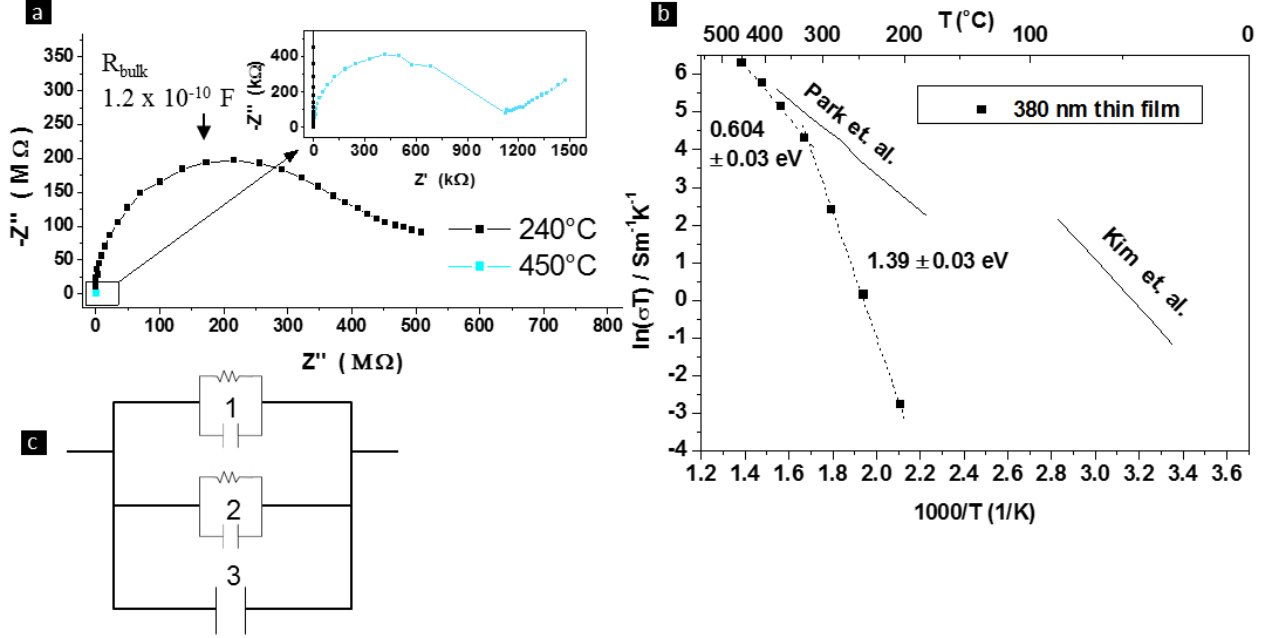


Fig. 5 a) Electrochemical impedance spectroscopy measured at 240°C and an inset at 450°C for 380 nm lithium post treated film. b) Arrhenius type plot of 380 nm films with activation energies included. References are provided for comparison. c) Circuit model used to describe the trend seen in the Arrhenius plot. Component 1 representing the oxygen ion conductivity of the  $\text{La}_2\text{Zr}_2\text{O}_7$  phase, 2 representing lithium ion conductivity in the  $\text{Li}_7\text{La}_3\text{Zr}_2\text{O}_{12}$ , and 3 representing the capacitance of the MgO substrate.